The Earth's surface controls the depth-dependent seismic radiation of megathrust earthquakes

Jiuxun Yin[1], **Marine A. Denolle**[1,2]

[1]Department of Earth and Planetary Sciences, Harvard University
[2]Department of Earth and Space Sciences, University of Washington

Key Points:

- Megathrust earthquakes radiate low-frequency updip and high-frequency downdip and such observation is ubiquitous.
- The interaction between the Earth free surface and the rupture is the first-order explanation for such depth-frequency relation.
- Realistic Earth structure is a second-order factor that further enhances the depth-frequency relation.

Corresponding author: Jiuxun Yin, jiuxun_yin@g.harvard.edu

Abstract

Megathrust earthquakes exhibit a ubiquitous seismic radiation style: low-frequency (LF) seismic energy is efficiently emitted from the shallowest portion of the fault, whereas high-frequency (HF) seismic energy is efficiently emitted from the deepest part of the fault. Although this is observed in many case-specific studies, we show that it is ubiquitous in global megathrust earthquakes between 1995 and 2021. Previous studies have interpreted this as an effect of systematic depth variation in either the plate interface frictional properties (Lay et al., 2012) or the P wavespeeds (Sallarès & Ranero, 2019). This work suggests an alternative hypothesis: the interaction between waves and ruptures due to the Earth's free surface is the leading mechanism that generates this behavior. Two-dimensional dynamic rupture simulations of subduction zone earthquakes support this hypothesis. Our simulations show that the interaction between the seismic waves reflected at the Earth's free surface and the updip propagating rupture results in LF radiation at the source. In contrast, the downdip propagation of rupture is less affected by the free surface and is thus dominated by HF radiation typical of buried faults. To a second degree, the presence of a realistic Earth structure derived from P-wave velocity (V_P) tomographic images and realistic V_P/V_S ratio estimated in boreholes further enhances the contrast in source radiation. We conclude that the Earth's free surface is necessary to explain the observed megathrust earthquake radiation style, and the realistic structure of subduction zone is necessary to better predict earthquake ground motion and tsunami potential.

Plain Language Summary

The largest earthquakes occur on the megathrusts of subduction zones and generate huge ground motions and devastating tsunami waves that threaten the coastal populations. Global databases of earthquake seismic signals reveal that almost all megathrust earthquakes have a particular radiation style. The shallow portion of the megathrust is where the seismic event generates tsunamis but low-frequency, less damaging ground motions, whereas deeper segments of the megathrust are where the rupture excites the high-frequency and destructive ground motion strongly felt by the nearby coastal and urban regions. The scientific community has focused on a depth dependence of fault-surface properties. This study instead shows that a dynamic feedback between seismic waves and rupture with the Earth's surface and realistic structures is sufficient to explain these observed phenomena.

1 Introduction

The largest and most damaging earthquakes occur offshore in subduction zones: the Mw 9.4 1960 Great Chilean earthquake, the 1964 Mw 9.3 Great Alaskan earthquake, the Mw 9.2 2004 Sumatra earthquakes, and the Mw 9.0 2011 Tohoku-oki earthquake. Because almost 1 in 10 people in the world live on the coast, understanding the rupture behavior of megathrust earthquakes is critical for seismic and tsunami risk mitigation in coastal areas. The recent occurrence of multiple of these events has coincided with a vast expansion in seismic networks, which, in turn, has led to the discovery of a multitude of processes surrounding the rupture of these large earthquakes (e.g., Ishii et al., 2005; Lay et al., 2012, and references therein).

A remarkable observation of these earthquakes' seismic signature is that low-frequency (LF) seismic waves are mostly generated at the shallow, updip region, while high-frequency (HF) seismic waves tend to come from the deep, downdip part. We refer to this as the "depth-frequency relation" in this work. It is manifested in three ways. First, studies on earthquake source time functions highlight a shortening of the source pulse that is well explained by an increase in elastic moduli with depth (Bilek & Lay, 1999; Houston, 2001; Vallée, 2013) and an increase in the relative contributions of HF radiation at depth

and along the megathrust (Ye et al., 2016; Chounet & Vallée, 2018). Second, the strong ground motions that are responsible for damaging urban infrastructure have been observed to originate from the downdip end of the megathrust (Kurahashi & Irikura, 2011; Asano & Iwata, 2012; Frankel, 2013). The third class of seismic observations is the back-projection (BP) image reconstructed from teleseismic P waves (Ishii et al., 2005). The BP image is effectively a blurred representation of the slip history on the fault (Fukahata et al., 2014; Yin & Denolle, 2019). Consequently, the images constructed at various frequency bands relate to the slip function's whole-event spectral content on the fault. Event-specific studies have shown that high frequencies are more efficiently generated at the downdip portion of the megathrust rather than its updip end (Kiser et al., 2011; Meng et al., 2011; Simons et al., 2011; Sufri et al., 2012; Yao et al., 2013; Melgar et al., 2016; Yin et al., 2016, 2017, 2018).

Here, we show three examples of such images using an Improved Compressive Sensing BackProjection (imCS-BP) method (Yao et al., 2011; Yin et al., 2018) for the Mw 9.0 2011 Tohoku-oki earthquake (D. Wang & Mori, 2011; Yao et al., 2011; Lay et al., 2012), the Mw 7.9 2015 Gorkha earthquake (Avouac et al., 2015; Yue et al., 2016; Yin et al., 2017), and the Mw 8.3 2015 Chilean Illapel earthquake (Melgar et al., 2016; Yin et al., 2016). We show both the LF and HF BP images in Fig. 1a - c. Supporting Information (Text S1, Figs. S1 - S3) provide additional details about data processing and results. These images clearly illustrate that HF source signals are emitted at greater depths than LF source signals.

We then turn to global databases of BP images provided by The Incorporated Research Institutions for Seismology (IRIS) over all the Mw 6.5+ earthquakes since 1995 (Incorporated Research Institutions for Seismology Data Management Center, 2011). Here, we select 461 earthquakes between 1995 and 2021 within the latitude-longitude range of the available Slab2 plate interface model (Hayes et al., 2018). We then project the HF and LF BP peaks of each earthquake onto the Slab2 model and calculate the corresponding HF and LF centroid depths. The centroid depth is a weighted average of the BP peak depths, the weights being the amplitude of BP peaks. Finally, we select the 245 earthquakes that have a BP centroid depth shallower than 70 km. For most earthquakes, especially the large magnitude ones with a likelihood of better time and spatial resolution of the BP image, we find that the centroid depth of the HF BP peaks is systematically greater than that of the LF peaks (Fig. 1d and Fig. S4). Two events stand out as exceptions: the Mw 9.0 2011 Tohoku-oki earthquake and the Mw 8.3 2006 Kuril Island earthquake (Ammon et al., 2008). For the 2011 Tohoku-oki earthquake, the exception is due to the different choice of frequency bands by the IRIS database, and we have shown that the refined BP results clearly present the depth-frequency relation (Fig. 1a, or figures in Yao et al. (2011)).

A common interpretation for these observations is the systematic depth variation in frictional properties that result from increasing temperature and pressure with depth and associated phase transformation of the minerals that compose the downgoing oceanic lithosphere. The argument is that systematic depth variations in fault properties can explain the evolution of the seismicity rates with depth (Scholz, 1998). It has also been widely used to explain the depth-varying seismic radiation of large megathrust earthquakes (Lay et al., 2012; Yao et al., 2013; Yin et al., 2017). Studies that simulate the dynamic rupture have adopted this with a parameterization of pre-stress or fault strength heterogeneity in the deeper portion of the seismogenic megathrust and have successfully reproduced HF and LF's relative contributions in seismic radiation (Huang et al., 2012; Galvez et al., 2014). Other studies have shown that it may be explained by a depth dependence in fault rheology, whereby the transition of frictional behaviors occurs, result in HF radiation at the rupture front (e.g., Noda & Lapusta, 2013; Michel et al., 2017). A recent alternative interpretation is that the systematic increase in P wavespeed (V_P) with depth in subduction zones directly impacts the wavelength and frequency of seismic waves emit-

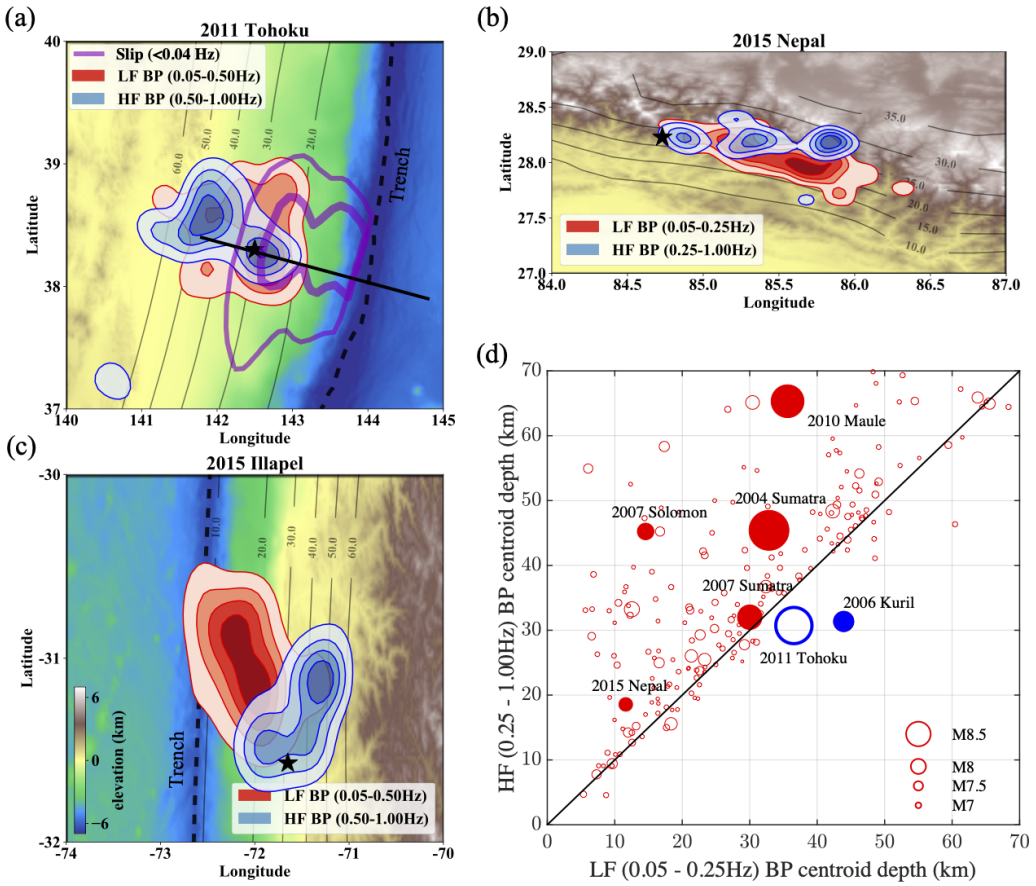

Figure 1. Ubiquitous depth-frequency relation found by back-projection observations. (a)-(c) BP images of the Mw 9.0 2011 Tohoku-oki, the Mw 7.9 2015 Gorkha, and the Mw 8.3 2015 Illapel earthquakes, respectively. The BP images are reconstructed using the imCS-BP method developed by Yin et al. (2018), and only the contours of 20%, 40%, 60%, and 80% maximum power are shown. The dashed black lines indicate the trench. The thin gray contours show the Slab2 model (Hayes et al., 2018). The purple contours in (a) show the 20 m and 50 m of coseismic slip distribution during the 2011 Tohoku earthquake from Lay et al. (2012), and the black solid line shows the location of the velocity profile of Miura et al. (2005). (d) Centroid depths of the low-frequency (0.05 - 0.25 Hz) BP images compared with the high-frequency (0.25 - 1 Hz) BP images from 245 M > 6.5 earthquakes.

ted at the source (Sallarès & Ranero, 2019). However, such an argument would also pertain to earthquakes in a wide depth range and from other tectonic environments. But we do not observe it for deeper earthquakes in the IRIS database (see Fig. S5).

Another major impact on megathrust earthquake dynamics is the asymmetrical fault-surface geometry: a shallow dipping fault intersects the Earth's free surface, and the accretionary and frontal wedge materials (hanging wall) are highly compliant compared to the footwall materials. This particular structure tends to trap seismic waves within the wedge and cause significant dynamic stress perturbations (Brune, 1996; Nielsen, 1998; Oglesby et al., 2000; Ma & Beroza, 2008; Guo et al., 2016; Gabuchian et al., 2017; Lotto et al., 2017, 2018; Tal et al., 2020). Such high stresses can lead to material yield-

ing (Ma & Hirakawa, 2013; Ma & Nie, 2019) or unclamping and flapping of the hanging wall (Brune, 1996; Gabuchian et al., 2017; Tal et al., 2020).

This study evaluates the impact of realistic structures in subduction zones, including the free surface and heterogeneous velocity structure, on the rupture dynamics and seismic radiation of megathrust earthquakes. We use two-dimensional (2D) dynamic models to investigate the radiation style of these earthquakes. A similar exercise was undertaken by Lotto et al. (2017, 2018), albeit a simplification of the 2D elastic structure and a focus on fault rheology and tsunamigenesis. Instead, this contribution uses a tomography-derived elastic model, a realistic model of the shear wavespeed (V_S), and provides a comprehensive analysis of the seismic waves generated by these ruptures.

Our results show that all simulations that contain a traction-free surface can reproduce the observations: HF seismic waves are more efficiently generated at depth, LF seismic waves are more efficiently generated near the trench. We define the **free-surface effects** as the dynamic interactions between the rupture and the seismic waves reflected from the surface. We propose that the **free-surface effects are the first-order explanation to the observed depth-frequency relation**. Furthermore, the subduction of a cold and wet slab produces a strong material contrast across the plate interface or fault, which favors the evolution of pulse-dominated rupture front and enhances high-frequency strong ground motions from the downdip region near the coast. Because such realistic velocity models exacerbate the contrast in radiation style, we propose that **realistic heterogeneous Earth velocity models give a significant second-order effect on controlling the seismic radiation**. We conclude that realistic Earth structures are necessary to predict tsunami and coastal ground motion hazards better.

2 Methods

We perform a set of dynamic rupture experiments in 2D media of small and large earthquakes. Five models are dedicated to small earthquakes in a simple homogeneous half space on a flat fault. For the rest, we gradually increase structural complexity from homogeneous to realistic elastic structures. By building up complexity, we explore to what degree the realism in Earth models impact the rupture. Combining different parameter settings, we obtained 29 representative rupture models. For both the small and large megathrust rupture models, we analyze the spectral properties of the rupture slip history. We further investigate the nearby ground motions and the tsunami potential for those megathrust models.

2.1 Representing a realistic megathrust structure

We choose the Tohoku region in northeastern Japan as our study case. We start from a benchmark case in the homogeneous full-space medium without free surface. Then we increase the complexity of the medium from a homogeneous half-space with a planar shallow dipping fault (11.8° degrees, Fig. 2a) to a heterogeneous half-space with realistic geometry and a regional V_P structure from Miura et al. (2005) (Fig. 1a and Fig. 2b). The elastic structure varies considerably along the dip of the megathrust, especially V_P in the upper plate (Sallarès & Ranero, 2019). Another aspect of the structural complexity is the high compliance of the sediments that constitute the accretionary wedge (Von Huene et al. (2009), and references therein). Here, we describe the megathrust fault zone into two canonical fault zone structures: 1) the updip fault zone has low-velocity properties and high V_P/V_S ratio, a nearby free surface, and a wide damaged zone, and 2) the downdip fault zone has a sharp contrast in material properties across the fault.

We focus our efforts to model a realistic updip region (above 20 km) on generating a realistic V_S structure. The compilation of V_P/V_S ratio values provided by Brocher (2005) suggests that low V_P materials have high V_P/V_S ratios. In light of this, we dis-

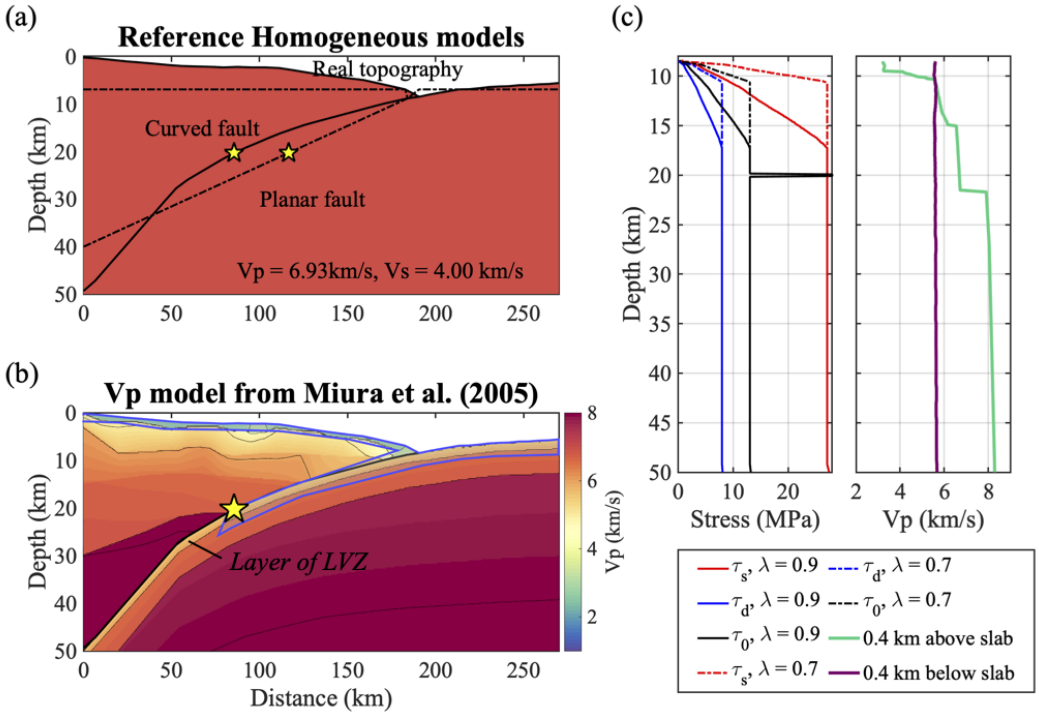

Figure 2. Model setting. (a) Model configuration in the homogeneous structure: a flat half-space with planar slab/fault geometry and a flat topography (dashed lines), a half-space with realistic slab geometry and seafloor topography (solid lines, referred to later as REF), hypocentral locations (yellow stars). (b) Heterogeneous half-space with realistic seafloor topography and V_P structure from Miura et al. (2005). The shaded blue areas highlight where V_P/V_S ratio is varied. (c) Fault properties: static strength levels τ_s (red), dynamic strength levels τ_d (blue), initial shear stress τ_0 (black) with different values of pore-pressure ratio λ of 0.7 (dashed lines) and 0.9 (solid lines), V_P along with two profiles projected at 400-m above (green) and 400-m below the plate interface (purple).

cuss three regions of possibly elevated V_P/V_S ratios. The first region is the subduction channel, the thin upper layer of the downgoing slab that is composed of fluid-rich seafloor sediments (Saffer & Tobin, 2011; Hicks et al., 2014; Naif et al., 2015; Zhu et al., 2020) and hydrated minerals in a mafic fractured crust (Shelly et al., 2006; Hicks et al., 2014; Bostock, 2013; Nishimura et al., 2019; Pimienta et al., 2018). The second region is the slope apron, the thin layer of the seafloor sediments that covers the wedge, which is best accessed by offshore drilling and active seismic surveys (Peacock et al., 2010; Tsuji et al., 2011; Fujie et al., 2013; Zhu et al., 2020). The third region we consider is the frontal prism that is the tip of the accretionary wedge where dragging of high V_P/V_S ratio sediments may occur (Saffer & Tobin, 2011; Fujie et al., 2013; Hicks et al., 2014; Nakamura et al., 2014). Due to the range of V_P/V_S values found in the literature, we vary the ratios between $\sqrt{3}$ ~1.73, 1.83, 1.94, 2.04, 2.14, 2.24, 2.35, and 2.45 in the three specific regions discussed above (Fig. S6). Although higher values have been reported within layers of seafloor sediments (Zhu et al., 2020), these are likely too thin to be resolved by our numerical exercise.

We now focus our attention on modeling material contrasts at the plate interface in the downdip region (between 20 and 50 km depth). Although the downgoing oceanic plate is denser than the overriding plate, the several-kilometer thin upper portion of the

oceanic crust exhibits low seismic velocities. It is present in most subduction zones and is referred to as the Low-Velocity Zone (LVZ). To confirm this common feature of subduction zones, we compile the range of V_P in the LVZ and across the fault in the upper plate in Supplementary Materials Table S1.

Finally, we embed the realistic structure in a homogeneous half-space and generate a larger simulation domain to avoid artifacts from the absorbing boundary conditions. We impose a 5-km smoothing operator to taper off velocity changes between the realistic structural model and the homogeneous half-space (Supporting Information Figure S7).

2.2 Modeling the dynamic rupture

The other ingredients necessary to model earthquake ruptures are fault properties such as the stress field, the pore pressure, and the frictional conditions (Fig. 2c). We explore several frictional conditions. In most models, we apply linear slip weakening on the entire fault. We test for slip-neutral and slip-strengthening conditions in the upper $\sim$ 10 km of the along-dip direction, in a zone of low-grade metamorphism where neutrally stable conditions may occur (Huang et al., 2012; Kozdon et al., 2013; Noda & Lapusta, 2013; Lotto et al., 2017, 2018). We also test the frictional constitutive relation proposed by Murphy et al. (2018) that is derived from laboratory experiments. In addition to increasing the V_P/V_S ratio, the fluid content also affects the stress fields by reducing overburden lithostatic pressure σ_L with pore fluid pressure p. We use the pore pressure ratio λ defined in Hubbert and Rubey (1959) to impose a pore pressure $p = \lambda\sigma_L$ as well as the effective normal stress $\bar{\sigma}_n = (1-\lambda)\sigma_L$. Given the uncertainties in λ, we test two values of λ (0.7 and 0.9) and assume that the pore fluid pressure becomes lithostatic when $\bar{\sigma}_n = 40$ MPa (Fig. 2d). These conditions are similar to those discussed and imposed in previous studies (e.g., Rice, 1992; Saffer & Tobin, 2011; Murphy et al., 2018; Lotto et al., 2018). The earthquake rupture naturally evolves on the fault in response to an over-stressed nucleation patch (see Fig. 2c). A full description of all model parameters is in Supporting Information (Text S2). We use the SEM2DPACK software (Ampuero, 2012, `https://github.com/jpampuero/sem2dpack`, last accessed on 06/08/2021) to simulate both the dynamic slip on the fault and the wavefield in the two-dimensional elastic domain.

2.3 Parameterization of the source radiation

To understand the relative contributions between LF and HF seismic waves emitted by the rupture, we parameterize the local slip-rate function's spectrum and improve from the qualitative discussions in Figure 3c of Ma and Hirakawa (2013) and Figure 12d of Galvez et al. (2014). In this study, we systematically measure and compare the along-dip spectral variations with two metrics.

The first approach fits the Fourier amplitude spectrum of the local slip-rate function with a flat model at low frequencies and a power-law decay at high frequencies. We apply a model commonly used in source seismology, $S(f) = 1/\left(1 + (f/f_c)^n\right)$, where f_c and n are the corner frequency and spectral falloff rate, respectively. The spectral model fits the shape of far-field P-wave pulses that originate from circular crack ruptures with uniform stress drop and elliptical slip distribution (Eshelby, 1957; Brune, 1970; Madariaga, 1976). It is common to perform spectral fitting over the spectrum of the far-field body-wave pulse of the entire event, which is the moment-rate pulse (Abercrombie & Rice, 2005; Allmann & Shearer, 2009; Trugman & Shearer, 2017; W. Wang & Shearer, 2019). Slip rate functions and overall moment-rate functions differ because the latter is the spatial integration of the former. This leads to differences in spectral shapes. For instance the slip-rate spectral shape may be sensitive to the breakdown time (Tinti et al., 2005; Huang, Ampuero, & Kanamori, 2014). We use this spectral shape solely to characterize the spec-

tral shapes and relative HF-LF content. The corner frequency f_c is inversely proportional to the pulse duration, which is also referred to as "rise time" in the kinematic representation of the earthquake source. The spectral falloff rate n describes how fast the high-frequency component decays in amplitude. The two spectral parameters trade off each other during the spectral fitting (Denolle & Shearer, 2016; Trugman & Shearer, 2017). Combining both can help to quantify the relative portions of LF and HF seismic radiation: larger f_c and smaller n correspond to relatively more HF radiation, while smaller f_c and larger n correspond to relatively more LF radiation. We apply a non-linear least-square solver to find f_c and n from fitting the $\log_{10}$ of the amplitude spectra of the local slip-rate functions interpolated on a logspace frequency vector, a strategy similar to other observational studies (see Shearer et al. (2019) for a recent review).

The second measure of relative contribution in frequency content estimates the seismic power generated by the local slip-acceleration function. Similar methods have been applied in previous studies to quantify the spectral power of slip rate from different frequency components (Huang et al., 2012; Huang, Ampuero, & Kanamori, 2014; Michel et al., 2017). Here we choose slip acceleration as the ground motion unit because far-field velocity seismograms are commonly used for teleseismic P-wave back-projection studies (Fukahata et al., 2014; Yin & Denolle, 2019) and are proportional to moment accelerations. We estimate the power by bandpassing (Butterworth, four corners, zero phase) and integrating the squared time series of local slip-acceleration functions in two frequency bands below the resolvable frequency: for small earthquake rupture in the homogeneous medium (Section 3.1), LF 0.001-0.1 Hz and HF 0.1 - 1 Hz; for megathrust rupture (Section 3.2), LF 0.001-0.06 Hz and HF 0.06 - 0.3 Hz. The central frequencies 0.1 Hz and 0.06 Hz are arbitrarily chosen as approximately the middle of the log-scale frequency band, but other tested values did not affect the general trends in the results. Details about the frequency resolution are in the Supporting Materials (Text S2.4). We then use the HF and LF seismic powers, specifically the HF/LF power ratio, to measure their relative contributions.

3 Results from dynamic rupture simulations

3.1 Cases of small subduction zone earthquakes

We start by inquiring whether the model setup can reproduce the differences in pulse width and fall-off rate that are reported from observations of small subduction-zone events (Houston, 2001; Ye et al., 2016). We systematically model five small ruptures initiated at the depths of 13.4 km, 17.6 km, 21.7 km, 25.9 km, and 30.0 km in a homogeneous structure with a planar fault and flat, free surface (Fig. 2a and Fig. S8). We impose pre-stress conditions to constrain the rupture length and keep other parameters equal in all simulations (see Fig. S8). Finally we apply our parameterizations to quantify the contributions from LF and HF radiation for these rupture models. Any difference in rupture style may then be attributed to free-surface effects controlled by the depth (or distance from the free surface) at which the rupture occurs.

The simulation results show that only the two shallower ruptures have reached the surface while the three deeper ones remain buried (Fig. 3a, Fig. S9). As the shallow ruptures reach the trench, they interact with the scattered wavefield. Such wave-rupture interaction disappears in the case of a source deeper than 20 km as the rupture almost terminates before the arrival of free-surface reflections (Fig. S9). Effectively, the deep sources are in a full-space. The shallow ruptures end up releasing about twice the moment (per unit of fault width) of the deep ruptures (Fig. 3a) due to the "mirror effect" from free surface (Luo et al., 2018).

Next, we fit the overall moment-density-rate function with the spectral model mentioned in Section 2.3 up to a resolvable frequency 1 Hz (Fig. 3c). This is in practice very

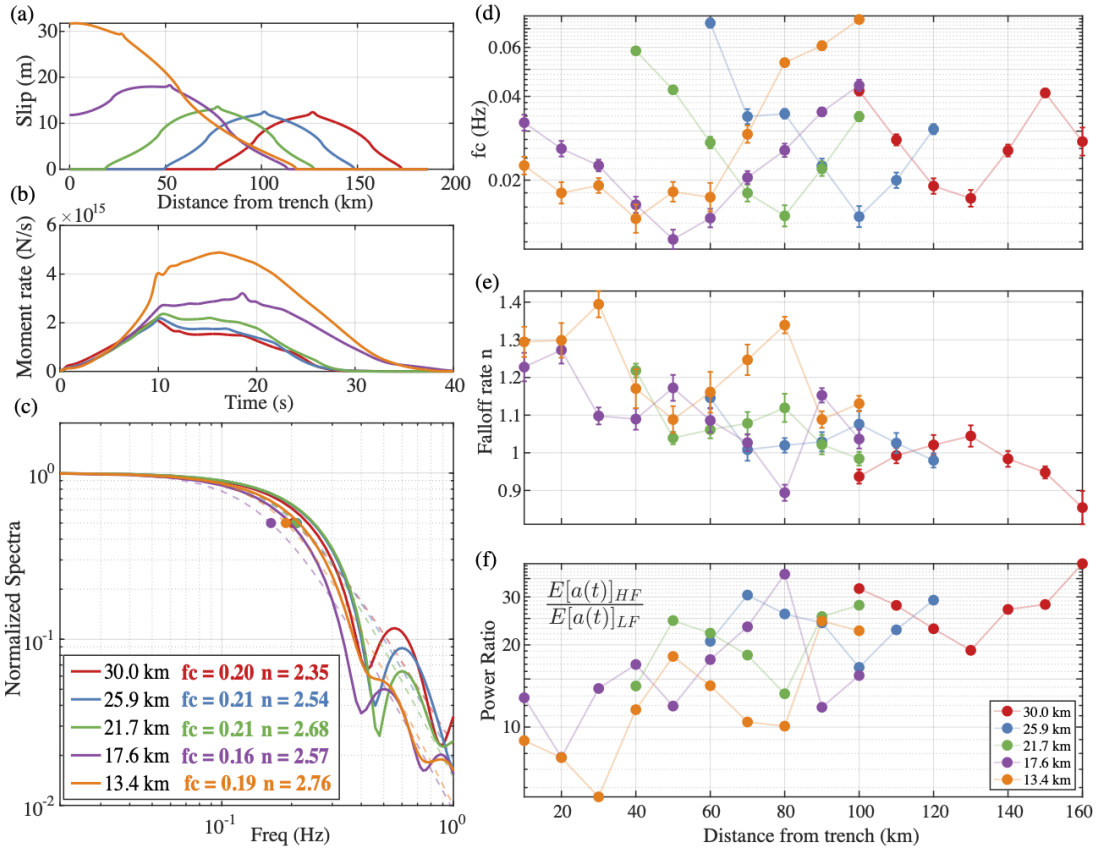

Figure 3. Simulation results of small megathrust earthquakes at different depths. (a) Final slip distributions on fault; (b) Moment-rate functions (per unit length along strike) averaged over the entire fault; (c) Amplitude-normalized source spectra (solid lines) as well as the corresponding best-fitted spectral models (dashed lines). The dots indicate the values of corner frequency f_c. (d)-(e) Best-fitted parameters of the slip rate functions at different depths for all the models: corner frequency f_c, spectral falloff rate n and HF/LF power ratio of slip acceleration, respectively.

similar to the seismological studies that explore earthquake source parameters (e.g., Abercrombie & Rice, 2005; Baltay et al., 2014; Denolle & Shearer, 2016; Trugman & Shearer, 2017). However, here we only use this model to quantify the spectral shape and avoid any dynamic implications on source parameters due to the circular-crack assumption of this spectral model (Eshelby, 1957; Brune, 1970; Madariaga, 1976). The spectral analysis shows that the source spectra of the two shallow earthquakes have lower $f_c = 0.19$ Hz and $f_c = 0.16$ Hz than the deeper ones with f_c about 0.2 Hz because of the longer duration of shallow ruptures. We also find a systematic trend of the spectral falloff rate n that the value of n systematically decreases along depth (Fig. 3c), implying that the moment-rate spectrum is more depleted in HF waves than deep earthquakes.

Moreover, we investigate how the local slip-rate functions vary with depth for each model. Details of the space-time rupture evolution can be found in Supplementary Figure S9. Here, we select an individual slip-rate function every 10 km along with the plate interface and measure corner frequency f_c, falloff rate n, and the corresponding HF/LF power ratio (Fig. 3d - f). There is no evident systematic along-depth variation of f_c; instead, it varies with the distance from the nucleation site as expected from crack mod-

els (rise time is longest at the nucleation patch). However, we find systematic along-depth variations of n and HF/LF power ratio: n decreases while HF/LF power ratio increases with depth for all models in general. Both n and the HF/LF ratio suggest that more HF components are radiated during the deeper ruptures. Since the only difference between the models is the source depths, i.e., the distances from the free surface, we suggest that free-surface effects are the origin of the depth-frequency relation.

3.2 Cases of megathrust earthquakes

In this section, we present our simulation results of the large megathrust earthquake models. Examples of the space-time evolution from the ruptures in the homogeneous full-space model (Full), homogeneous half-space model (REF) and heterogeneous model (V_P/V_S = 2.04 in the V_P/V_S-elevated regions) are shown in Figure 4a. Our half-space simulations are typical of 2D models of dynamic rupture (Huang et al., 2012; Kozdon et al., 2013; Lotto et al., 2017; Ramos & Huang, 2019). All simulated ruptures reach the trench, last about 60 seconds, and their final slip increases from small downdip to large updip. The rupture first propagates bilaterally from its nucleation patch. The updip rupture then hits the trench with a high slip rate, and a weak re-rupture front propagates back downdip. The downdip rupture propagates with a constant rupture velocity and dies at the end of the fault. The slip profiles along the dip (Fig. 5) are similar to many of those inferred for the Mw 9.0 2011 Tohoku-oki earthquake (summarized in K. Wang et al., 2018, and references therein). By comparison, the simulation in the homogeneous full-space model presents symmetric rupture behavior at the updip and downdip propagating fronts. The slight asymmetry of full-space model is due to the initial stress distribution (Fig. 4a and Fig. 5b). We refer to Supporting Information 2 for each model's detailed results and summarize their general patterns.

To explore the depth-varying properties, we apply the same parameterization in previous sections to all megathrust rupture models (Fig. 6). First, we perform the spectral fitting for each slip-rate function. We find that all models with a free surface present similar along-dip (or depth) variations of the spectral properties (Fig. 6a and Fig. S10). The spectral falloff rate n generally decreases with depth: it is about 1.8 - 2.0 (model median) on the shallow segment from 0 - 20 km and 0.8 - 1.0 (model median) on the deep segment. Second, we calculate the HF/LF power ratio of slip accelerations in the HF (0.06 - 0.3 Hz) and LF (0.001 - 0.06 Hz) bands. Here again, we find a clear pattern that the HF/LF power ratio increases with depth (down-dip) for all those half-space models (Fig. 6b). We also repeat the measurements for the segment-averaged slip-rate functions (on the 10-km subfaults), and the patterns stay the same (Fig. S11).

In all free-surface models, both measures of the local slip-rate functions' relative frequency content vary systematically with depth. Such systematic variation contrasts with the results obtained with the full-space model's case: both the spectral falloff rate n and the HF/LF ratio remain constant (Fig. 6) because of the symmetry of slip history (Figs. 4-5). This is consistent with the results from the small subduction-zone megathrust earthquakes in Section 3.1, and again suggests that **free-surface effects are the first-order mechanism that explains the frequency-depth radiation during megathrust earthquakes**. Furthermore, we notice that the rupture models in the realistic heterogeneous mediums present stronger contrast in radiation style, that is stronger variations of falloff rate n and HF/LF power ratio with depth than the models in the homogeneous structure. It means that the **realistic velocity structure can be a second-order mechanism and further enhance the observations of depth-frequency relation**.

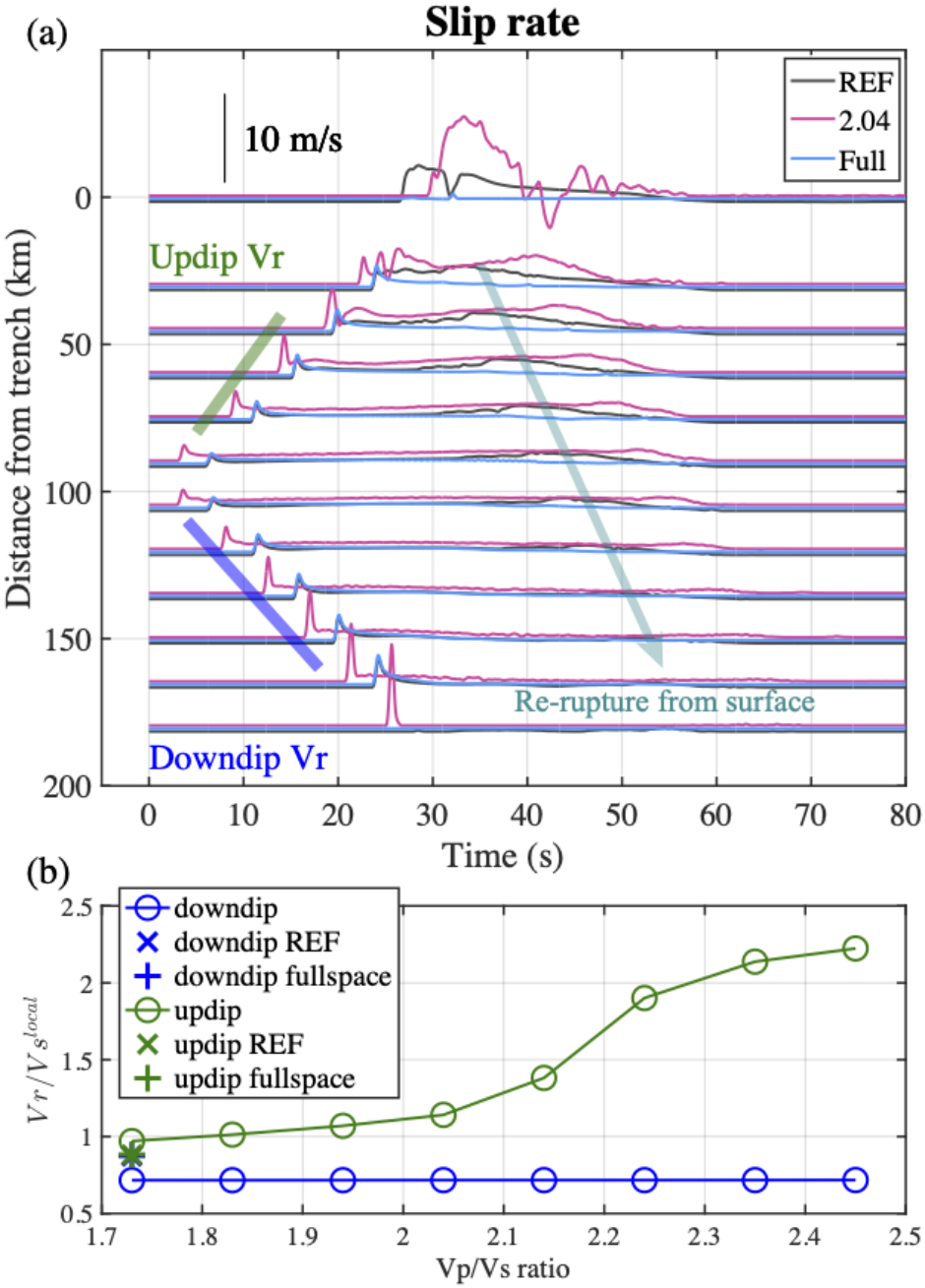

Figure 4. Space-time evolution of the simulated megathrust earthquake. Comparisons of simulation result from the model in heterogeneous medium with V_P/V_S=2.04 (Fig. 2b) and homogeneous models: REF model with real topography in Figure 2a (dark gray) and full-space model (light blue). (a) Space-time slip-rate evolution: green and blue lines crudely mark the updip and downdip rupture front; the gray-blue arrow indicates the weak re-rupture propagating downdip from the surface. The pore pressure ratio λ=0.9 in this comparison. (b) Rupture speeds of updip (in green, 40 km to 80 km from the trench) and downdip (in blue, 110 km to 160 km from the trench) propagation for each model. V_S^{local} is chosen based on the P wave velocity 0.4 km above slab (green line in Fig. 2c) and the V_P/V_S ratio in each model.

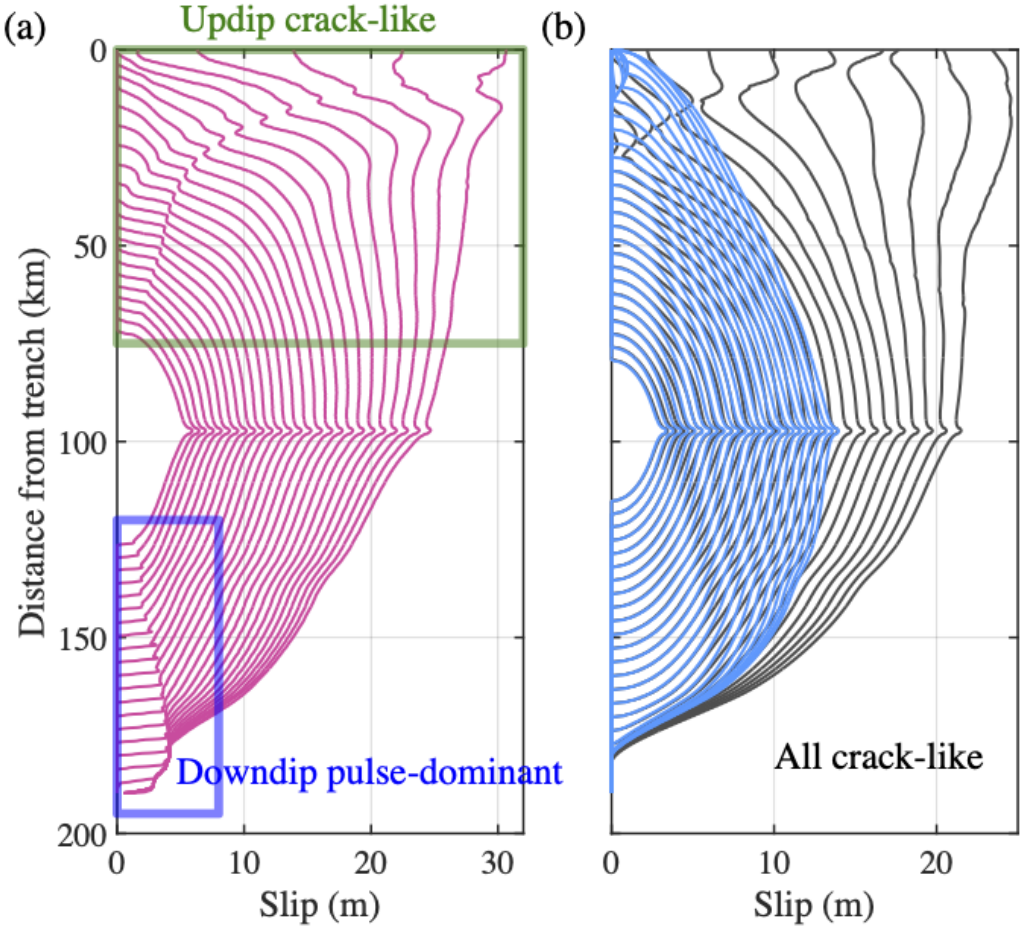

Figure 5. Slip history of the simulated earthquakes. Snapshots of slip distribution from (a) models with heterogeneous velocity structures and V_P/V_S=2.04; (b) homogeneous models in half-space with real topography (dark gray) and in full-space (blue). Slip contours from every second between 10 to 35 s are plotted.

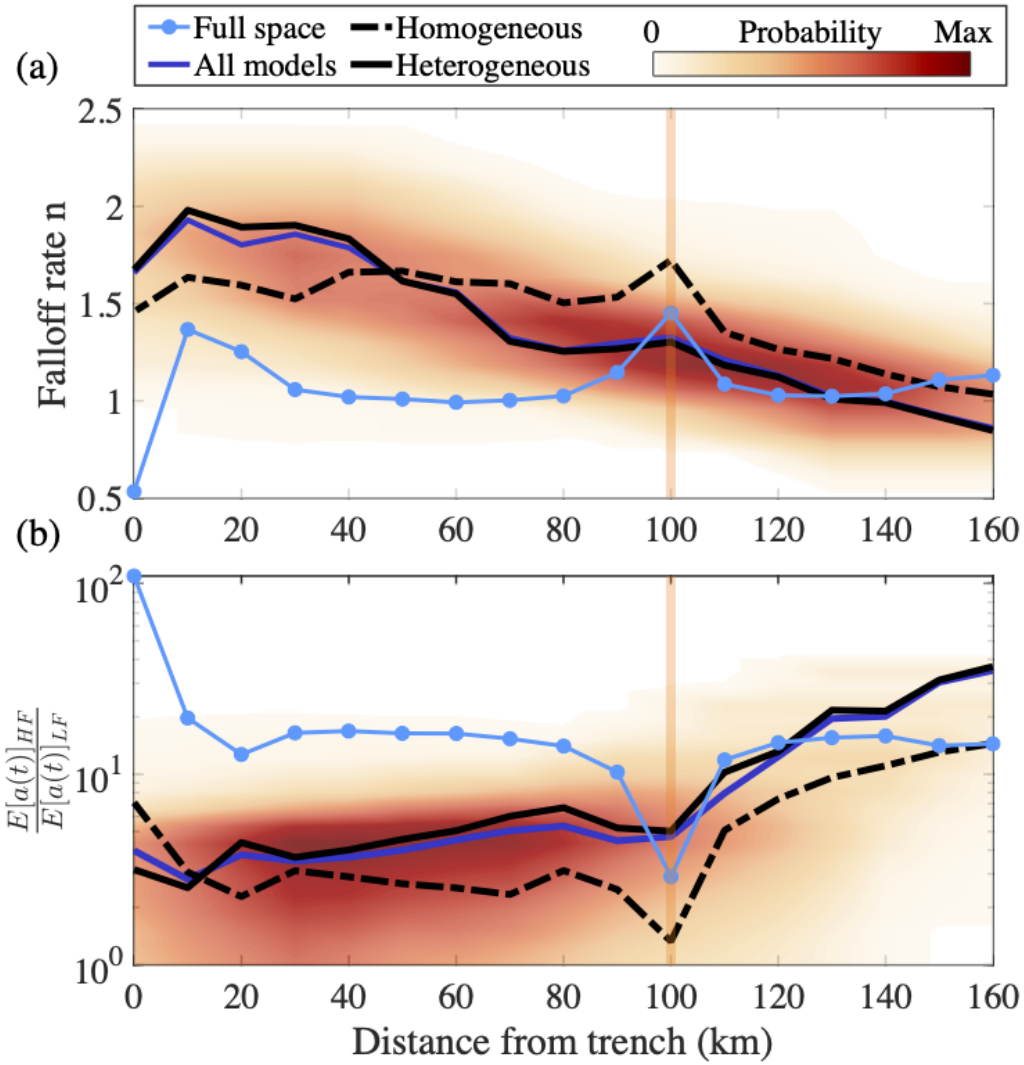

Figure 6. Spectral properties of the source radiation, shown by the probability distribution from all models. These distributions are obtained from the Box-kernel smoother. (a) Best-fitted spectral falloff rate n along dip from the simulated megathrust earthquake with different model settings. (b) The power ratio of high frequency (HF) 0.06 - 0.3 Hz and low frequency (LF) 0.001 - 0.06 Hz slip acceleration along dip. Dark blue solid line shows the median value of all models. Black dashed line and solid line show the median values from all homogeneous models and all heterogeneous models, respectively. The light blue dotted line shows the result from the homogeneous full-space model. The orange bar indicate the location of rupture nucleation.

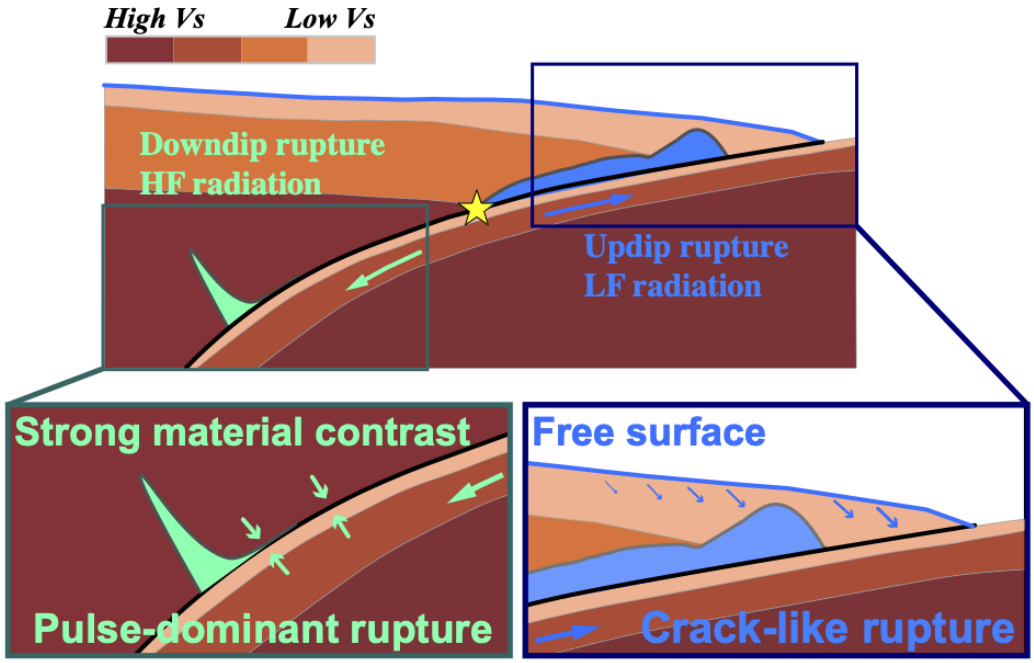

Figure 7. Effects of the free surface and material contrasts on the dynamic behavior of megathrust earthquakes. In the updip region, the free surface leads to crack-like rupture (slip-rate distribution is shown in blue) and enhanced low-frequency radiation. In the downdip part, the substantial material contrast at the top of the LVZ favors pulse-dominant rupture (slip-rate distribution is shown in green) and enhanced high-frequency seismic radiation.

4 Discussion

This study focuses on the effects of free surface and realistic Earth structure on the dynamic rupture behavior of megathrust earthquakes. While we test one particular subduction zone in northeastern Japan (Miura et al., 2005), the overall structure exists in many other subduction zones (Table S1). Three specific structural features appear to impact the depth-frequency relation of megathrust earthquakes (Fig. 7): 1) the free surface in the near-source region, 2) the high compliance of the sediments in the updip wedge, and 3) the low-velocity zone below the plate interface downdip. Our systematic simulations show that free-surface effects are the first-order mechanism, and the heterogeneity in material compliance further enhances the radiation contrast. We illustrate this in Figure 7. We now discuss the varied rupture behavior, their impact on the depth-frequency relation, and further implication for ground motion and tsunami hazards.

4.1 Updip rupture: large and fast crack rupture to the trench

The rupture accelerates updip and evolves as a crack (Fig. 5): the shallow rupture velocities are higher than typically observed (Chounet et al., 2018) and greater than the surrounding V_S, and slip continues until the end of rupture. Our simulations shed light on two major factors that control this updip behavior: the free surface and the shallow compliant fault zone.

Previous studies have shown that the free surface can significantly change the normal stress during rupture, due to waves reflecting at the free surface and traveling back

to the fault (Brune, 1996; Nielsen, 1998; Oglesby et al., 1998, 2000; Y. Wang et al., 2019; Tal et al., 2020). Our simulation results are no different: clear surface-reflected phases cause the prolonged and persistent slip in the updip portion (Supporting Information 2). Free-surface effects also induce acceleration of rupture propagation with supershear velocity: a secondary "daughter crack" can be triggered by the surface-reflected shear wave, which can be seen in other studies (Huang et al., 2012; Lotto et al., 2017) and in other tectonic regimes such as strike-slip earthquakes (Kaneko & Lapusta, 2010). The "mirror effect" of the free surface to seismic waves can also cause larger coseismic slip even with a constant stress drop value (Luo et al., 2018).

The highly compliant structure of the shallow hanging wall of the megathrust acts as a seismic waveguide. The upper plate low-velocity sediments can trap seismic waves, amplify their amplitudes and extend their duration. This wave propagation effect is similar to how seismic waves amplify when traveling in sedimentary basins (Campillo et al., 1989). Despite differences in model settings, all simulations show that the initial wave emitted at the rupture front, the free-surface reflections, and other wedge captured and scattered waves interfere together to energize rupture propagation and further increase the final slip. In our simulations, these normal stress changes and fault-parallel slip are so extreme, with peak slip rates on the order of 10 m/s, that some models with standard V_P/V_S ratios predict co-seismic backslip (Fig. 4a). In simulations with higher V_P/V_S ratios, much lower V_S may delay the propagation of scattered waves in a way that limits their constructive interference back to the fault. Regardless, such extreme values of slip rates generate large dynamic stresses that can cause (not modeled) inelastic failure (Ma & Hirakawa, 2013; Ma & Nie, 2019), wedge flapping (Brune, 1996; Gabuchian et al., 2017). This phenomenon may be the cause for the suggested dynamic overshoot during the Mw 9.0 2011 Tohoku-oki earthquake (Ide et al., 2011).

Moreover, the downgoing plate is fractured and hydrated on the foot-wall side with low velocities and elevated V_P/V_S ratios (10 - 20 km depth in Fig. 2b). Altogether, the structure is similar to that observed in crustal damage zones (Ben-Zion & Sammis, 2003). Harris and Day (1997) suggested that the low-velocity structure around the fault can affect the rupture speed and slip-velocity pulse shape. Furthermore, such a low-velocity structure dramatically impacts rupture propagation and termination, such as multiple slip pulses, supershear rupture velocity, and rotation of background stress (Rubin & Ampuero, 2007; Ampuero & Ben-Zion, 2008; Huang, Ampuero, & Helmberger, 2014; Huang, 2018).

In the homogeneous case with a uniform V_P/V_S ratio of $\sqrt{3}$ and realistic fault and seafloor geometries (REF model in Fig. 6 and Fig. 8), the rupture velocity for both updip and downdip rupture has a typical value of $0.87V_S$. In the models that have realistic V_P/V_S ratios, the updip rupture velocity becomes greater than the local V_S. This is typical for 2D elastic models of earthquakes on the megathrust of subduction zones (Lotto et al., 2018) and in damaged fault zones (Huang, Ampuero, & Helmberger, 2014; Weng et al., 2016; Huang et al., 2016).

4.2 Downdip rupture: pulse-dominant rupture along with the LVZ

As the rupture propagates to the downdip region, there is no impact from free-surface reflections as the rupture ends before waves travel back to the fault. All models present a sharp rupture front (Fig. 4a). In the models with a homogeneous structure, the slip-rate functions have typical long tails (Kostrov, 1964). In the models with heterogeneous structures, the slip-rate functions are characterized by a shortening of the slip pulse (stronger healing) with depth (or along dip with hypocentral distance). In both situations, our quantification on the spectrum shows that the HF energy dominates due to the impulsive slip-rate function shape.

The material contrast across the fault can explain the evolution of short and sharp slip pulses downdip of the hypocenter. Theoretical studies have predicted the slip pulse produced by the material contrast at the fault interface (Weertman, 1980; Andrews & Ben-Zion, 1997). Moreover, Shlomai and Fineberg (2016) perform and analyze lab experiments with an in-plane shear of the two blocks with different compliance. They show that such a bimaterial interface can host both rupture modes: one self-healing slip pulse that moves in one direction of rupture and one slip crack that propagates in the opposite direction. The experimental configuration is similar to that of the subduction zones downdip of the seismogenic zone with the contact between the LVZ and the overhanging upper mantle material. As the rupture propagates downdip, in the moving direction of the more compliant oceanic plate, the slip-rate functions are short and sharp pulses (Fig. 4a). The corresponding downdip rupture speed V_r is about 0.71 V_S^{local} (Fig. 4b), which is the local shear wavespeed of the continental crust near the slab (Fig. 2c), but is about 5% higher than the shear wavespeed in the LVZ. This has also been shown by the experiments of Shlomai and Fineberg (2016).

Previous theoretical and numerical studies show that the generation of a self-healing slip-pulse on bimaterial interface required specific conditions of initial stress, friction or geometry (Shi & Ben-Zion, 2006; Rubin & Ampuero, 2007; Ampuero & Ben-Zion, 2008; Olsen-Kettle et al., 2008; Dalguer & Day, 2009). This study has not covered the parameterization of those conditions for our dynamic models of megathrust rupture. But we leave them as a future direction to explore in combination with theoretical studies and constraints on how fault is localized in subduction zones from geological observations.

4.3 Depth-frequency relation of megathrust earthquakes

In this study, we have shown that all earthquakes simulated in half-spaces exhibit similar along-dip (along-depth) variations in the values of the spectral parameters and HF/LF ratios of the local slip-rate functions (Fig. 3, Fig. 6), which is consistent with the observed depth-frequency relation (Fig. 1). In contrast, the benchmark full-space simulation is not consistent with the observations. Therefore, we propose that free-surface effects are the first-order factor in explaining the observed depth-frequency relation of megathrust earthquakes.

The cases of the simulated small earthquake ruptures reveal that the shallower earthquakes are more depleted in high-frequency radiation than the deeper ones (Fig. 3). These patterns are consistent with the observed systematic depth variations of source parameters for small-to-moderate earthquakes(Houston, 2001; Ko & Kuo, 2016; Denolle & Shearer, 2016; Ye et al., 2016). The depletion in HF content is mainly caused by the interference between direct rupture and the free-surface reflection (Fig. S9).

The cases of the simulated large earthquake ruptures further support the claim that free-surface effects are the leading factor to explain the depth-frequency relation during large megathrust earthquakes. The deep portion of the rupture has elevated HF radiation compared to the shallow portion, regardless of model setting (Fig. 6). Our study suggests that a crack-like rupture mode exemplifies the updip rupture of megathrust earthquakes. In contrast, the sharp slip-pulses are the dominant mode of the downdip ruptures, at least as seen by seismic radiation (Fig. 4a).

This study focuses on the Tohoku region, however our results are generalizable since the free-surface dominate the response. We also tested a shallow vertical mode-III (anti-plane) rupture in a homogeneous halfspace and found a similar patterns in the spectral content (Fig. S12). These findings imply that the depth-frequency relation may also exist for other types of earthquakes such as strike-slip events at shallow depth. However, there is no observation of such phenomenon, which we attribute to the poor resolution with depth using teleseismic waves. Improvements in the Green's function for near surface source may help find the seismic signatures.

Moreover, models that include realistic velocity structures exhibit a stronger variations in n and HF/LF ratios with depth (Fig. 6). We attribute this stronger contrast to the wave effects in a realistic velocity structure. First, the shallow, compliant, high-V_P/V_S accretionary wedge trap waves more effectively, slows their propagation, and increase the duration of slip on the fault, which enhances LF radiation near the trench. Second, the deep strong material contrast between the LVZ and the continental, overriding mantle can lead to more pulse-dominant slip histories with more HF radiation in the downdip region. Therefore, the realistic elastic structure in the subduction zone is another controlling factor to the depth-varying frequency-dependence of seismic radiation.

4.4 Implications for tsunami and ground motion hazards

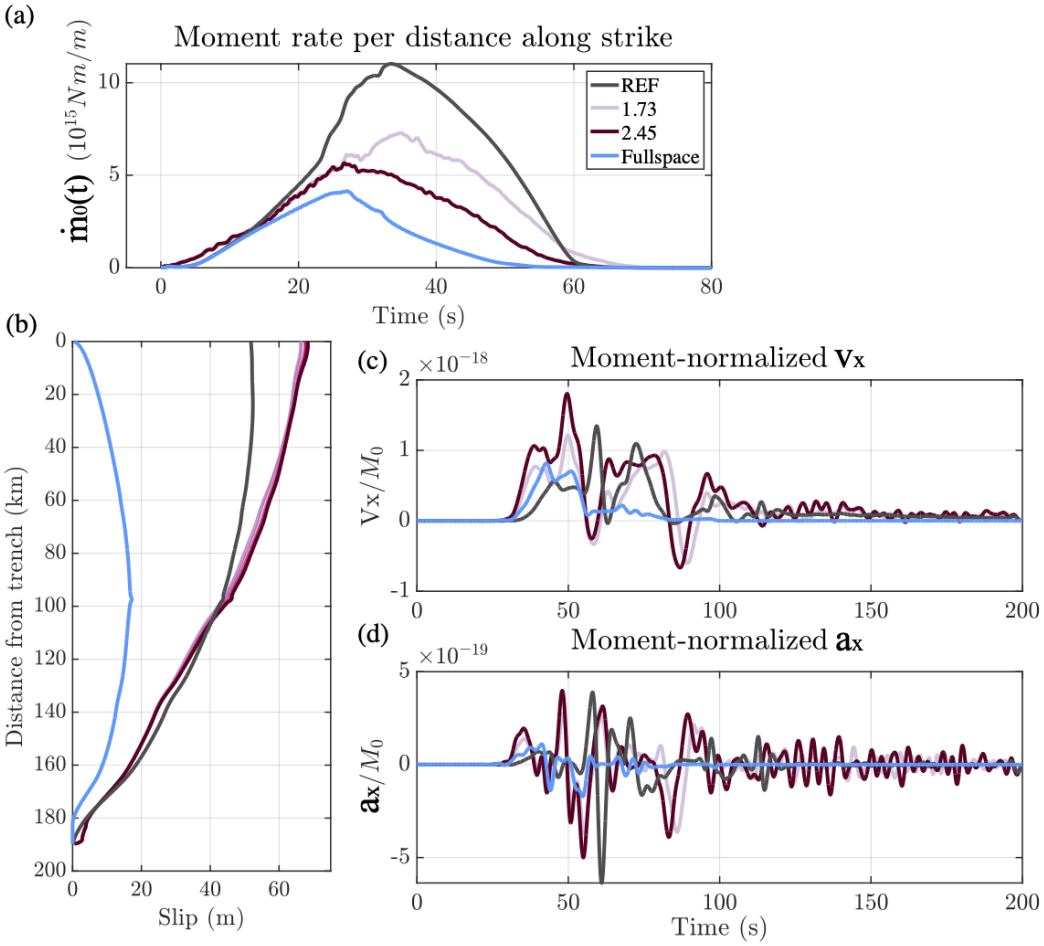

Figure 8. Tsunami and ground motion hazards. (a) Moment-rate density function of each model with different V_P/V_S ratios. (b) Final along-dip slip distribution from different models. (c) Moment-normalized velocity seismograms (horizontal x direction) recorded by the far-field station (location shown in Fig. S7b). (d) Corresponding moment-normalized acceleration seismograms (horizontal x-direction) recorded by the same virtual station.

Our simulations indicate that the final slip distribution varies considerably with the model settings. The final moment magnitude of the homogeneous half-space models is larger than the heterogeneous models, probably due to the greater shear modulus

at the shallow portion (Fig. 8a). However, the final slip is greater underneath shallow and highly compliant structures (Fig.8b), which was also found by Lotto et al. (2018). The final slip at the trench directly impacts the tsunami height. We apply a simplified relation from Tanioka and Satake (1996) to estimate the initial tsunami height at the trench: $\eta_{ts} = u_y - m u_x$, where u_x, u_y, and $m = -0.1$ are the horizontal displacement, vertical displacement, and the horizontal gradient of the bathymetry at the trench, respectively. We find that $\eta_{ts} = 8.6$ m for the homogeneous half-space model (REF model), 11.0 m for the heterogeneous model with $V_P/V_S = \sqrt{3}$ and 11.3 m for the heterogeneous model with $V_P/V_S = 2.45$. This simple exercise reaffirms the results from previous studies that the realistic velocity structure, especially the shallow V_S structure, is necessary to estimate better the potential tsunami hazards (Lotto et al., 2018).

We also compare the ground motions that would be recorded at a station in the coastal region (Fig. 8c-d and Fig. S7). The strong ground motions that are responsible for damaging urban infrastructure may arrive as distinct high-frequency bursts from the downdip part of the megathrust (Kurahashi & Irikura, 2011; Asano & Iwata, 2012; Frankel, 2013). Moment-normalized velocity and acceleration seismograms produced by the different models of this study have relatively similar peak amplitudes. The earliest peak amplitudes of ground motions occur when the rupture hits the trench. However, the duration of strong shaking is much greater in realistic structures. We attribute this to the wave reverberation in the wedge (wave propagation effects) and not a source effect since the source duration is comparable (~ 60 s). The presence of the LVZ naturally increases the strong ground motion hazard: it is located nearby the coastal regions and tends to produce three times more HF seismic power than in reference, uniform models (Fig.6). Previous studies have illustrated the existence of distinct strong-motion generation areas (SMGAs) (Kurahashi & Irikura, 2011; Asano & Iwata, 2012; Frankel, 2013). The SMGAs imply that there may be heterogeneity in the LVZ such that the spatial variations in elastic structure may control variations in slip-front healing (i.e., more or less healing of the slip pulse). These can also be modeled by heterogeneity in fault properties (Huang et al., 2012).

5 Conclusion

Global databases of BP images show a systematic depth variation of the frequency content in source radiation. While this finding was discussed in Lay et al. (2012) for several large events, here we show that it is a systematic pattern among most moderate-to-large subduction zone earthquakes. This study provides a simple and generalizable explanation of this observation. We find that the inclusion of Earth's free surface is sufficient to explain this ubiquitous observation. We propose that the dynamics of shallow rupture are dominated by free-surface effects that are, in turn, the first-order factor in explaining the depth-frequency relation. The second-order effect is the evolution of earthquake rupture in a realistic velocity structure that is typical of shallow subduction zones (< 50 km), one that has a compliant wedge and a low-velocity zone atop the downgoing slab. The presence of anomalously low V_S, relative to V_P, also impacts the rupture behavior that further enhance the depth-dependence of seismic radiation. Furthermore, our findings resonate with previous work that realistic structures are necessary to correctly model tsunami and ground motion hazards in future subduction zone earthquakes (Lotto et al., 2018). Because elastic wavespeed properties are likely better constrained than frictional properties at depth, our study promotes the use of tomographic images in dynamic rupture modeling and ground motion predictions.

There are several key limitations to this work and avenues to improve upon it. Free-surface effects consist of multiple factors including fault geometry/curvature, depth of earthquake rupture, seafloor topography, bulk properties, which could be explored in a rather systematic way in future analysis. Our preliminary attempts to produce a synthetic backprojection by coupling the dynamic rupture models using SPECFEM2D (Tromp

et al., 2008) failed due to a poor resolution of the BP peaks in the 2D dynamic modeling setting. Part of this limitation is likely due to the 2D modeling against 3D modeling, which would provide more spatial dimension to separate the BP peaks. 3D realistic structure effects may matter more for the along-strike propagation of rupture, which is not explored in this setting. We have also ignored the water layer, though this should not affect too much the rupture process (Kozdon et al., 2013). We also have not included inelastic rheology, which would smooth the slip evolution at the trench and further enhance the depth-frequency relation (Ma & Hirakawa, 2013; Ma & Nie, 2019). These are fantastic avenues for future work.

Acknowledgments

We sincerely thank Seiichi Miura at JAMSTEC (Japan Agency for Marine-Earth Science and Technology) for providing the velocity model of the Japan trench. We are grateful to Yihe Huang, Alice-Agnes Gabriel and Alexander Hutko for their constructive and productive discussions. We appreciate the insightful comments, which have greatly improved the manuscript, from the three reviewers, Yongfei Wang, Jean-Paul Ampuero and another anonymous reviewer. We are grateful to Jean-Paul Ampuero for developing SEM2DPACK (available at `https://github.com/jpampuero/sem2dpack`). The back-projection results used in Figure 1 (a) are downloaded from IRIS data services products: back-projection (`https://ds.iris.edu/ds/products/back-projection/`, last accessed on 02/27/2021). The Slab2 model is downloaded from U.S. Geological Survey (`https://www.sciencebase.gov/catalog/item/5aa1b00ee4b0b1c392e86467`, last accessed on 02/27/2021). All the down-sampled simulation results and relevant scripts are in Figshare (`https://figshare.com/projects/The_Earth_surface_controls_the_depth-dependent_seismic_radiation_of_megathrust_earthquakes/98360`) for result reproduction. This work is supported by the CAREER EAR-1749556 NSF award).

References

Abercrombie, R. E., & Rice, J. R. (2005). Can observations of earthquake scaling constrain slip weakening? *Geophysical Journal International*, *162*(2), 406–424. doi: 10.1111/j.1365-246X.2005.02579.x

Allmann, B. P., & Shearer, P. M. (2009). Global variations of stress drop for moderate to large earthquakes. *Journal of Geophysical Research: Solid Earth*, *114*(B1), B01310. doi: 10.1029/2008JB005821

Ammon, C. J., Kanamori, H., & Lay, T. (2008). A great earthquake doublet and seismic stress transfer cycle in the central Kuril islands. *Nature*, *451*(7178), 561–565. doi: 10.1038/nature06521

Ampuero, J. P. (2012). SEM2DPACK, a spectral element software for 2D seismic wave propagation and earthquake source dynamics, v2.3.8. Retrieved from `https://doi.org/10.5281/zenodo.230363` (More information at https://github.com/jpampuero/sem2dpack) doi: 10.5281/zenodo.230363

Ampuero, J.-P., & Ben-Zion, Y. (2008). Cracks, pulses and macroscopic asymmetry of dynamic rupture on a bimaterial interface with velocity-weakening friction. *Geophysical Journal International*, *173*(2), 674–692. doi: 10.1111/j.1365-246X.2008.03736.x

Andrews, D. J., & Ben-Zion, Y. (1997). Wrinkle-like slip pulse on a fault between different materials. *Journal of Geophysical Research: Solid Earth*, *102*(B1), 553–571. doi: 10.1029/96JB02856

Asano, K., & Iwata, T. (2012). Source model for strong ground motion generation in the frequency range 0.1–10 Hz during the 2011 Tohoku earthquake. *Earth, Planets and Space*, *64*(12), 6. doi: 10.5047/eps.2012.05.003

Avouac, J.-P., Meng, L., Wei, S., Wang, T., & Ampuero, J.-P. (2015). Lower edge of locked Main Himalayan Thrust unzipped by the 2015 Gorkha earthquake. *Na-*

ture Geoscience, *8*(9), 708–711. doi: 10.1038/ngeo2518

Baltay, A. S., Beroza, G. C., & Ide, S. (2014). Radiated Energy of Great Earthquakes from Teleseismic Empirical Green's Function Deconvolution. *Pure and Applied Geophysics*, *171*(10), 2841–2862. doi: 10.1007/s00024-014-0804-0

Ben-Zion, Y., & Sammis, C. G. (2003). Characterization of fault zones. *Pure and applied geophysics*, *160*(3), 677–715.

Bilek, S. L., & Lay, T. (1999). Rigidity variations with depth along interplate megathrust faults in subduction zones. *Nature*, *400*(6743), 443–446.

Bostock, M. G. (2013). The Moho in subduction zones. *Tectonophysics*, *609*, 547–557. doi: 10.1016/j.tecto.2012.07.007

Brocher, T. M. (2005, 12). Empirical Relations between Elastic Wavespeeds and Density in the Earth's Crust. *Bulletin of the Seismological Society of America*, *95*(6), 2081-2092. doi: 10.1785/0120050077

Brune, J. N. (1970). Tectonic stress and the spectra of seismic shear waves from earthquakes. *Journal of Geophysical Research*, *75*(26), 4997–5009. doi: 10.1029/JB075i026p04997

Brune, J. N. (1996). Particle motions in a physical model of shallow angle thrust faulting. *Proceedings of the Indian Academy of Sciences - Earth and Planetary Sciences*, *105*(2), 197. doi: 10.1007/BF02876014

Campillo, M., Gariel, J., Aki, K., & Sanchez-Sesma, F. (1989). Destructive strong ground motion in mexico city: Source, path, and site effects during great 1985 michoacán earthquake. *Bulletin of the Seismological Society of America*, *79*(6), 1718–1735.

Chounet, A., & Vallée, M. (2018). Global and interregion characterization of subduction interface earthquakes derived from source time functions properties. *Journal of Geophysical Research: Solid Earth*, *123*(7), 5831–5852.

Chounet, A., Vallée, M., Causse, M., & Courboulex, F. (2018). Global catalog of earthquake rupture velocities shows anticorrelation between stress drop and rupture velocity. *Tectonophysics*, *733*, 148–158. doi: 10.1016/j.tecto.2017.11.005

Dalguer, L. A., & Day, S. M. (2009). Asymmetric rupture of large aspect-ratio faults at bimaterial interface in 3D. *Geophysical Research Letters*, *36*(23). Retrieved from `https://agupubs.onlinelibrary.wiley.com/doi/abs/10.1029/2009GL040303` doi: 10.1029/2009GL040303

Denolle, M. A., & Shearer, P. M. (2016). New perspectives on self-similarity for shallow thrust earthquakes. *Journal of Geophysical Research: Solid Earth*, *121*(9), 2016JB013105. doi: 10.1002/2016JB013105

Eshelby, J. D. (1957). The determination of the elastic field of an ellipsoidal inclusion, and related problems. , *241*, 376–396.

Frankel, A. (2013). Rupture History of the 2011 M 9 Tohoku Japan Earthquake Determined from Strong-Motion and High-Rate GPS Recordings: Subevents Radiating Energy in Different Frequency BandsRupture History of the 2011 M 9 Tohoku Earthquake from Strong-Motion and High-Rate GPS Recordings. *Bulletin of the Seismological Society of America*, *103*(2B), 1290–1306. doi: 10.1785/0120120148

Fujie, G., Kodaira, S., Yamashita, M., Sato, T., Takahashi, T., & Takahashi, N. (2013). Systematic changes in the incoming plate structure at the Kuril trench. *Geophysical Research Letters*, *40*(1), 88–93. doi: https://doi.org/10.1029/2012GL054340

Fukahata, Y., Yagi, Y., & Rivera, L. (2014). Theoretical relationship between back-projection imaging and classical linear inverse solutions. *Geophysical Journal International*, *196*(1), 552–559. doi: 10.1093/gji/ggt392

Gabuchian, V., Rosakis, A. J., Bhat, H. S., Madariaga, R., & Kanamori, H. (2017). Experimental evidence that thrust earthquake ruptures might open faults. *Nature*, *545*(7654), 336–339.

Galvez, P., Ampuero, J.-P., Dalguer, L. A., Somala, S. N., & Nissen-Meyer, T. (2014). Dynamic earthquake rupture modelled with an unstructured 3-D spectral element method applied to the 2011 M9 Tohoku earthquake. *Geophysical Journal International*, *198*(2), 1222–1240. doi: 10.1093/gji/ggu203

Guo, Y., Koketsu, K., & Miyake, H. (2016). Propagation mechanism of long-period ground motions for offshore earthquakes along the nankai trough: Effects of the accretionary wedge. *Bulletin of the Seismological Society of America*, *106*(3), 1176–1197.

Harris, R. A., & Day, S. M. (1997). Effects of a low-velocity zone on a dynamic rupture. *Bulletin of the Seismological Society of America*, *87*(5), 1267–1280.

Hayes, G. P., Moore, G. L., Portner, D. E., Hearne, M., Flamme, H., Furtney, M., & Smoczyk, G. M. (2018). Slab2, a comprehensive subduction zone geometry model. *Science*, *362*(6410), 58–61. doi: 10.1126/science.aat4723

Hicks, S. P., Rietbrock, A., Ryder, I. M., Lee, C.-S., & Miller, M. (2014). Anatomy of a megathrust: The 2010 M8. 8 Maule, Chile earthquake rupture zone imaged using seismic tomography. *Earth and Planetary Science Letters*, *405*, 142–155. doi: 10.1016/j.epsl.2014.08.028

Houston, H. (2001). Influence of depth, focal mechanism, and tectonic setting on the shape and duration of earthquake source time functions. *Journal of Geophysical Research: Solid Earth*, *106*(B6), 11137–11150. doi: 10.1029/2000JB900468

Huang, Y. (2018). Earthquake Rupture in Fault Zones With Along-Strike Material Heterogeneity. *Journal of Geophysical Research: Solid Earth*, *123*(11), 9884–9898. doi: https://doi.org/10.1029/2018JB016354

Huang, Y., Ampuero, J.-P., & Helmberger, D. V. (2014). Earthquake ruptures modulated by waves in damaged fault zones. *Journal of Geophysical Research: Solid Earth*, *119*(4), 3133–3154. doi: 10.1002/2013JB010724

Huang, Y., Ampuero, J.-P., & Helmberger, D. V. (2016). The potential for supershear earthquakes in damaged fault zones–theory and observations. *Earth and Planetary Science Letters*, *433*, 109–115.

Huang, Y., Ampuero, J.-P., & Kanamori, H. (2014). Slip-Weakening Models of the 2011 Tohoku-Oki Earthquake and Constraints on Stress Drop and Fracture Energy. *Pure and Applied Geophysics*, *171*(10), 2555–2568. doi: 10.1007/s00024-013-0718-2

Huang, Y., Meng, L., & Ampuero, J.-P. (2012). A dynamic model of the frequency-dependent rupture process of the 2011 Tohoku-Oki earthquake. *Earth, Planets and Space*, *64*(12), 1. doi: 10.5047/eps.2012.05.011

Hubbert, M. K., & Rubey, W. W. (1959). Role of fluid pressure in mechanics of overthrust faulting: I. mechanics of fluid-filled porous solids and its application to overthrust faulting. *GSA Bulletin*, *70*(2), 115–166. doi: 10.1130/0016-7606(1959)70[115:ROFPIM]2.0.CO;2

Ide, S., Baltay, A., & Beroza, G. C. (2011). Shallow dynamic overshoot and energetic deep rupture in the 2011 mw 9.0 tohoku-oki earthquake. *Science*, *332*(6036), 1426–1429.

Incorporated Research Institutions for Seismology Data Management Center. (2011). Data Services Products: BackProjection P-wave back-projection rupture imaging.
doi: 10.17611/DP/BP.1.

Ishii, M., Shearer, P. M., Houston, H., & Vidale, J. E. (2005). Extent, duration and speed of the 2004 Sumatra–Andaman earthquake imaged by the Hi-Net array. *Nature*, *435*(7044), 933. doi: 10.1038/nature03675

Kaneko, Y., & Lapusta, N. (2010). Supershear transition due to a free surface in 3-D simulations of spontaneous dynamic rupture on vertical strike-slip faults. *Tectonophysics*, *493*(3), 272–284. doi: 10.1016/j.tecto.2010.06.015

Kiser, E., Ishii, M., Langmuir, C. H., Shearer, P. M., & Hirose, H. (2011). Insights into the mechanism of intermediate-depth earthquakes from source properties as imaged by back projection of multiple seismic phases. *Journal of Geophysical Research: Solid Earth*, *116*(B6), B06310. doi: 10.1029/2010JB007831

Ko, J. Y.-T., & Kuo, B.-Y. (2016). Low radiation efficiency of the intermediate-depth earthquakes in the Japan subduction zone. *Geophysical Research Letters*, *43*(22), 2016GL070993. doi: 10.1002/2016GL070993

Kostrov, B. V. (1964). Selfsimilar problems of propagation of shear cracks. *Journal of Applied Mathematics and Mechanics*, *28*(5), 1077–1087. doi: 10.1016/0021-8928(64)90010-3

Kozdon, J. E., Dunham, E. M., & Nordström, J. (2013). Simulation of Dynamic Earthquake Ruptures in Complex Geometries Using High-Order Finite Difference Methods. *Journal of Scientific Computing*, *55*(1), 92–124. doi: 10.1007/s10915-012-9624-5

Kurahashi, S., & Irikura, K. (2011). Source model for generating strong ground motions during the 2011 off the Pacific coast of Tohoku Earthquake. *Earth, Planets and Space*, *63*(7), 11. doi: 10.5047/eps.2011.06.044

Lay, T., Kanamori, H., Ammon, C. J., Koper, K. D., Hutko, A. R., Ye, L., ... Rushing, T. M. (2012). Depth-varying rupture properties of subduction zone megathrust faults. *Journal of Geophysical Research: Solid Earth*, *117*(B4), B04311. doi: 10.1029/2011JB009133

Lotto, G. C., Dunham, E. M., Jeppson, T. N., & Tobin, H. J. (2017). The effect of compliant prisms on subduction zone earthquakes and tsunamis. *Earth and Planetary Science Letters*, *458*, 213–222. doi: 10.1016/j.epsl.2016.10.050

Lotto, G. C., Jeppson, T. N., & Dunham, E. M. (2018). Fully Coupled Simulations of Megathrust Earthquakes and Tsunamis in the Japan Trench, Nankai Trough, and Cascadia Subduction Zone. *Pure and Applied Geophysics*. doi: 10.1007/s00024-018-1990-y

Luo, Y., Ampuero, J.-P., Miyakoshi, K., & Irikura, K. (2018). Surface Rupture Effects on Earthquake Moment-Area Scaling Relations. In L. A. Dalguer, Y. Fukushima, K. Irikura, & C. Wu (Eds.), *Best Practices in Physics-based Fault Rupture Models for Seismic Hazard Assessment of Nuclear Installations* (pp. 7–18). Cham: Springer International Publishing. doi: 10.1007/978-3-319-72709-7_2

Ma, S., & Beroza, G. C. (2008). Rupture Dynamics on a Bimaterial Interface for Dipping FaultsRupture Dynamics on a Bimaterial Interface for Dipping Faults. *Bulletin of the Seismological Society of America*, *98*(4), 1642–1658. doi: 10.1785/0120070201

Ma, S., & Hirakawa, E. T. (2013). Dynamic wedge failure reveals anomalous energy radiation of shallow subduction earthquakes. *Earth and Planetary Science Letters*, *375*, 113–122. doi: 10.1016/j.epsl.2013.05.016

Ma, S., & Nie, S. (2019). Dynamic wedge failure and along-arc variations of tsunamigenesis in the japan trench margin. *Geophysical Research Letters*, *46*(15), 8782-8790. doi: 10.1029/2019GL083148

Madariaga, R. (1976). Dynamics of an expanding circular fault. *Bulletin of the Seismological Society of America*, *66*(3), 639–666.

Melgar, D., Fan, W., Riquelme, S., Geng, J., Liang, C., Fuentes, M., ... Fielding, E. J. (2016). Slip segmentation and slow rupture to the trench during the 2015, Mw8.3 Illapel, Chile earthquake. *Geophysical Research Letters*, *43*(3), 2015GL067369. doi: 10.1002/2015GL067369

Meng, L., Inbal, A., & Ampuero, J.-P. (2011). A window into the complexity of the dynamic rupture of the 2011 Mw 9 Tohoku-Oki earthquake. *Geophysical Research Letters*, *38*(7), L00G07. doi: 10.1029/2011GL048118

Michel, S., Avouac, J.-P., Lapusta, N., & Jiang, J. (2017). Pulse-like partial ruptures and high-frequency radiation at creeping-locked transition during megath-

rust earthquakes. *Geophysical Research Letters*, *44*(16), 8345–8351. doi: https://doi.org/10.1002/2017GL074725

Miura, S., Takahashi, N., Nakanishi, A., Tsuru, T., Kodaira, S., & Kaneda, Y. (2005). Structural characteristics off Miyagi forearc region, the Japan Trench seismogenic zone, deduced from a wide-angle reflection and refraction study. *Tectonophysics*, *407*(3), 165–188. doi: 10.1016/j.tecto.2005.08.001

Murphy, S., Di Toro, G., Romano, F., Scala, A., Lorito, S., Spagnuolo, E., ... Nielsen, S. (2018). Tsunamigenic earthquake simulations using experimentally derived friction laws. *Earth and Planetary Science Letters*, *486*, 155–165. doi: 10.1016/j.epsl.2018.01.011

Naif, S., Key, K., Constable, S., & Evans, R. L. (2015). Water-rich bending faults at the Middle America Trench. *Geochemistry, Geophysics, Geosystems*, *16*(8), 2582–2597. doi: 10.1002/2015GC005927

Nakamura, Y., Kodaira, S., Cook, B. J., Jeppson, T., Kasaya, T., Yamamoto, Y., ... Fujie, G. (2014). Seismic imaging and velocity structure around the JFAST drill site in the Japan Trench: low V p, high V p/V s in the transparent frontal prism. *Earth, Planets and Space*, *66*(1), 121. doi: 10.1186/1880-5981-66-121

Nielsen, S. B. (1998). Free surface effects on the propagation of dynamic rupture. *Geophysical Research Letters*, *25*(1), 125–128. doi: 10.1029/97GL03445

Nishimura, K., Uehara, S., & Mizoguchi, K. (2019). An alternative origin of high vp/vs anomalies in slow slip regions: Experimental constraints from the elastic wave velocity evolution of highly fractured rock. *Journal of Geophysical Research: Solid Earth*, *124*(5), 5045–5059.

Noda, H., & Lapusta, N. (2013). Stable creeping fault segments can become destructive as a result of dynamic weakening. *Nature*, *493*(7433), 518–521. doi: 10.1038/nature11703

Oglesby, D. D., Archuleta, R. J., & Nielsen, S. B. (1998). Earthquakes on Dipping Faults: The Effects of Broken Symmetry. *Science*, *280*(5366), 1055–1059. doi: 10.1126/science.280.5366.1055

Oglesby, D. D., Archuleta, R. J., & Nielsen, S. B. (2000). Dynamics of dip-slip faulting: Explorations in two dimensions. *Journal of Geophysical Research: Solid Earth*, *105*(B6), 13643–13653.

Olsen-Kettle, L. M., Weatherley, D., Saez, E., Gross, L., Mühlhaus, H.-B., & Xing, H. L. (2008). Analysis of slip-weakening frictional laws with static restrengthening and their implications on the scaling, asymmetry, and mode of dynamic rupture on homogeneous and bimaterial interfaces. *Journal of Geophysical Research: Solid Earth*, *113*(B8). Retrieved from `https://agupubs.onlinelibrary.wiley.com/doi/abs/10.1029/2007JB005454` doi: 10.1029/2007JB005454

Peacock, S., Westbrook, G. K., & Bais, G. (2010). S-wave velocities and anisotropy in sediments entering the Nankai subduction zone, offshore Japan. *Geophysical Journal International*, *180*(2), 743–758. doi: 10.1111/j.1365-246X.2009.04430.x

Pimienta, L., Schubnel, A., Violay, M., Fortin, J., Guéguen, Y., & Lyon-Caen, H. (2018). Anomalous vp/vs ratios at seismic frequencies might evidence highly damaged rocks in subduction zones. *Geophysical Research Letters*, *45*(22), 12,210-12,217. doi: https://doi.org/10.1029/2018GL080132

Ramos, M. D., & Huang, Y. (2019). How the Transition Region Along the Cascadia Megathrust Influences Coseismic Behavior: Insights From 2-D Dynamic Rupture Simulations. *Geophysical Research Letters*, *46*(4), 1973–1983. doi: 10.1029/2018GL080812

Rice, J. R. (1992). Chapter 20 Fault Stress States, Pore Pressure Distributions, and the Weakness of the San Andreas Fault. In B. Evans & T.-f. Wong (Eds.), *International Geophysics* (Vol. 51, pp. 475–503). Academic Press. doi: 10.1016/

S0074-6142(08)62835-1

Rubin, A. M., & Ampuero, J.-P. (2007). Aftershock asymmetry on a bimaterial interface. *Journal of Geophysical Research: Solid Earth*, *112*(B5). doi: https://doi.org/10.1029/2006JB004337

Saffer, D. M., & Tobin, H. J. (2011). Hydrogeology and mechanics of subduction zone forearcs: Fluid flow and pore pressure. *Annual Review of Earth and Planetary Sciences*, *39*, 157–186.

Sallarès, V., & Ranero, C. R. (2019). Upper-plate rigidity determines depth-varying rupture behaviour of megathrust earthquakes. *Nature*, *576*(7785). doi: 10.1038/s41586-019-1784-0

Scholz, C. H. (1998). Earthquakes and friction laws. *Nature*, *391*(6662), 37–42. doi: 10.1038/34097

Shearer, P. M., Abercrombie, R. E., Trugman, D. T., & Wang, W. (2019). Comparing egf methods for estimating corner frequency and stress drop from p wave spectra. *Journal of Geophysical Research: Solid Earth*, *124*(4), 3966–3986.

Shelly, D. R., Beroza, G. C., Zhang, H., Thurber, C. H., & Ide, S. (2006). High-resolution subduction zone seismicity and velocity structure beneath Ibaraki Prefecture, Japan. *Journal of Geophysical Research: Solid Earth*, *111*(B6). doi: 10.1029/2005JB004081

Shi, Z., & Ben-Zion, Y. (2006). Dynamic rupture on a bimaterial interface governed by slip-weakening friction. *Geophysical Journal International*, *165*(2), 469–484. doi: 10.1111/j.1365-246X.2006.02853.x

Shlomai, H., & Fineberg, J. (2016). The structure of slip-pulses and supershear ruptures driving slip in bimaterial friction. *Nature Communications*, *7*(1). doi: 10.1038/ncomms11787

Simons, M., Minson, S. E., Sladen, A., Ortega, F., Jiang, J., Owen, S. E., ... Webb, F. H. (2011). The 2011 Magnitude 9.0 Tohoku-Oki Earthquake: Mosaicking the Megathrust from Seconds to Centuries. *Science*, *332*(6036), 1421–1425. doi: 10.1126/science.1206731

Sufri, O., Koper, K. D., & Lay, T. (2012). Along-dip seismic radiation segmentation during the 2007 Mw 8.0 Pisco, Peru earthquake. *Geophysical Research Letters*, *39*(8), L08311. doi: 10.1029/2012GL051316

Tal, Y., Rubino, V., Rosakis, A. J., & Lapusta, N. (2020). Illuminating the physics of dynamic friction through laboratory earthquakes on thrust faults. *Proceedings of the National Academy of Sciences*, *117*(35), 21095–21100.

Tanioka, Y., & Satake, K. (1996). Tsunami generation by horizontal displacement of ocean bottom. *Geophysical Research Letters*, *23*(8), 861–864. doi: 10.1029/96GL00736

Tinti, E., Fukuyama, E., Piatanesi, A., & Cocco, M. (2005). A Kinematic Source-Time Function Compatible with Earthquake Dynamics. *Bulletin of the Seismological Society of America*, *95*(4), 1211–1223. doi: 10.1785/0120040177

Tromp, J., Komatitsch, D., & Liu, Q. (2008). Spectral-element and adjoint methods in seismology. *Communications in Computational Physics*, *3*(1), 1-32.

Trugman, D. T., & Shearer, P. M. (2017). Application of an improved spectral decomposition method to examine earthquake source scaling in Southern California. *Journal of Geophysical Research: Solid Earth*, *122*(4), 2890–2910. doi: https://doi.org/10.1002/2017JB013971

Tsuji, T., Dvorkin, J., Mavko, G., Nakata, N., Matsuoka, T., Nakanishi, A., ... Nishizawa, O. (2011). VP/VS ratio and shear-wave splitting in the Nankai Trough seismogenic zone: Insights into effective stress, pore pressure, and sediment consolidationTsuji et al.VP/VS ratio & S-wave splitting from OBS data. *Geophysics*, *76*(3), WA71–WA82. doi: 10.1190/1.3560018

Vallée, M. (2013). Source time function properties indicate a strain drop independent of earthquake depth and magnitude. *Nature Communications*, *4*, 2606. doi: 10.1038/ncomms3606

Von Huene, R., Ranero, C. R., & Scholl, D. W. (2009). Convergent margin structure in high-quality geophysical images and current kinematic and dynamic models. In *Subduction zone geodynamics* (pp. 137–157). Springer.

Wang, D., & Mori, J. (2011). Frequency-dependent energy radiation and fault coupling for the 2010 Mw8.8 Maule, Chile, and 2011 Mw9.0 Tohoku, Japan, earthquakes. *Geophysical Research Letters*, *38*(22). doi: 10.1029/2011GL049652

Wang, K., Sun, T., Brown, L., Hino, R., Tomita, F., Kido, M., ... Fujiwara, T. (2018). Learning from crustal deformation associated with the M9 2011 Tohoku-oki earthquake. *Geosphere*, *14*(2), 552–571. doi: 10.1130/GES01531.1

Wang, W., & Shearer, P. M. (2019). An improved method to determine coda-q, earthquake magnitude, and site amplification: Theory and application to southern california. *Journal of Geophysical Research: Solid Earth*, *124*(1), 578–598. doi: https://doi.org/10.1029/2018JB015961

Wang, Y., Day, S. M., & Denolle, M. A. (2019). Geometric Controls on Pulse-Like Rupture in a Dynamic Model of the 2015 Gorkha Earthquake. *Journal of Geophysical Research: Solid Earth*, *124*(2), 1544–1568. doi: 10.1029/2018JB016602

Weertman, J. (1980). Unstable slippage across a fault that separates elastic media of different elastic constants. *Journal of Geophysical Research: Solid Earth*, *85*(B3), 1455–1461. doi: 10.1029/JB085iB03p01455

Weng, H., Yang, H., Zhang, Z., & Chen, X. (2016). Earthquake rupture extents and coseismic slips promoted by damaged fault zones. *Journal of Geophysical Research: Solid Earth*, *121*(6), 4446–4457. doi: 10.1002/2015JB012713

Yao, H., Gerstoft, P., Shearer, P. M., & Mecklenbräuker, C. (2011). Compressive sensing of the Tohoku-Oki Mw 9.0 earthquake: Frequency-dependent rupture modes. *Geophysical Research Letters*, *38*(20), L20310. doi: 10.1029/2011GL049223

Yao, H., Shearer, P. M., & Gerstoft, P. (2013). Compressive sensing of frequency-dependent seismic radiation from subduction zone megathrust ruptures. *Proceedings of the National Academy of Sciences*, *110*(12), 4512–4517. doi: 10.1073/pnas.1212790110

Ye, L., Lay, T., Kanamori, H., & Rivera, L. (2016). Rupture characteristics of major and great (mw 7.0) megathrust earthquakes from 1990 to 2015: 2. depth dependence. *Journal of Geophysical Research: Solid Earth*, *121*(2), 845–863.

Yin, J., & Denolle, M. A. (2019). Relating teleseismic backprojection images to earthquake kinematics. *Geophysical Journal International*, *217*(2), 729–747. doi: 10.1093/gji/ggz048

Yin, J., Denolle, M. A., & Yao, H. (2018). Spatial and Temporal Evolution of Earthquake Dynamics: Case Study of the Mw 8.3 Illapel Earthquake, Chile. *Journal of Geophysical Research: Solid Earth*, *123*(1), 344–367. doi: 10.1002/2017JB014265

Yin, J., Yang, H., Yao, H., & Weng, H. (2016). Coseismic radiation and stress drop during the 2015 Mw 8.3 Illapel, Chile megathrust earthquake. *Geophysical Research Letters*, *43*(4), 1520–1528. doi: 10.1002/2015GL067381

Yin, J., Yao, H., Yang, H., Qin, W., Jing, L.-Z., & Zhang, H. (2017). Frequency-dependent rupture process, stress change, and seismogenic mechanism of the 25 April 2015 Nepal Gorkha Mw 7.8 earthquake. *SCIENCE CHINA Earth Sciences*, *60*(4), 796–808. doi: 10.1007/s11430-016-9006-0

Yue, H., Simons, M., Duputel, Z., Jiang, J., Fielding, E., Liang, C., ... Samsonov, S. V. (2016). Depth varying rupture properties during the 2015 Mw 7.8 Gorkha (Nepal) earthquake. *Tectonophysics*. doi: 10.1016/j.tecto.2016.07.005

Zhu, J., Canales, J. P., Han, S., Carbotte, S. M., Arnulf, A., & Nedimović, M. R. (2020). Vp/vs ratio of incoming sediments off cascadia subduction zone from analysis of controlled-source multicomponent obs records. *Journal of Geophysical Research: Solid Earth*, *125*(6), e2019JB019239.